



# A universal framework for metropolis Monte Carlo simulation of magnetic Curie temperature



Yehui Zhang<sup>a</sup>, Bing Wang<sup>b</sup>, Yilv Guo<sup>a</sup>, Qiang Li<sup>a,\*</sup>, Jinlan Wang<sup>a,\*</sup>

<sup>a</sup> School of Physics, Southeast University, Nanjing 211189, China

<sup>b</sup> Institute for Computational Materials Science, School of Physics and Electronics, Henan University, Kaifeng 475004, China

## ARTICLE INFO

### Keywords:

Heisenberg model  
Monte Carlo methods  
Ferromagnetic materials  
Density functional theory (DFT)

## ABSTRACT

Recent research of two-dimensional magnetism intrigues rapidly growing attention and broadens the prospects for utility in nano-devices. However, understanding the new magnetic phenomena and the behavior of magnetic centers is still one of the challenges. The Heisenberg model with the Metropolis Monte Carlo method provides an accurate description with continuous degrees of freedom while effective and universal spin update algorithms remain highly desirable. In this study, we propose algorithms for the magnetization switching in the classical Heisenberg model based on the concept of Euler angles and quaternion, which update the spins simply by a rotation matrix and convert to sphere and Cartesian coordinates in a very convenient way. The proposed methods are fully tested and validated by comparisons with the benchmarks of both the two-dimensional square lattice Ising model and the three-dimensional cubic lattice Heisenberg model. As an application example of the two-dimensional ferromagnetic material of CrI<sub>3</sub>, the simulated Curie temperature is about 42 K, which is in good agreement with the experimental value of 45 K. The update algorithms together with other configuration schemes are compiled into an easy-to-operate program named SEU-mtc, aiming to execute post-processing analysis of the spin microstates and greatly improve the efficiency of Curie temperature simulations based on *ab initio* methods.

## 1. Introduction

Recently, magnetism in van der Waals (vdW) structures has attracted great attention because it provides a new possibility for realizing truly two-dimensional (2D) spintronic devices, which benefits by the properties of low energy consumption, fast device operation, and high storage density [1–10]. According to Mermin-Wagner theorem, no long-range magnetic ordering at finite temperatures would exist in 2D systems within the isotropic Heisenberg model with continuous spin symmetries [11]. Accordingly, the 2D isotropic classical Heisenberg model does not have long-range order and thus miss the Curie temperature. However, 2D ferromagnetic materials CrI<sub>3</sub> [1] and CrGeTe<sub>3</sub> [2] are experimentally synthesized recently, and the result indicates that magnetic anisotropy (MA) can break the continuous symmetry in the Mermin-Wagner theorem. Thanks to the mechanical and liquid exfoliation techniques, several vdW magnetic materials are found to be suitable to make 2D magnetism by reducing their thickness down to the monolayer limit [3–5]. More importantly, 2D magnetic crystals constitute ideal platforms for understanding the fundamental physics of

magnetism, the control of which has been fueling opportunities for atomically thin, magnetoelectric, and magneto-optic devices [12,13].

In fact, 2D magnetism has been investigated theoretically for decades while the experimental validation was unable to achieve until recently [14–18]. For example, single-layer VS<sub>2</sub> and VSe<sub>2</sub> were predicted to be intrinsic ferromagnets theoretically in 2012, which were verified by experiments after 2017 [19–23]. Besides, the recent synthesized ferromagnetic ultrathin Cr<sub>2</sub>Ge<sub>2</sub>Te<sub>6</sub>, CrI<sub>3</sub>, and Fe<sub>3</sub>GeTe<sub>2</sub> [1–3] were first predicted theoretically [24–26], which show the strong power of first-principles calculations. The MA, which can be scaled by the magnetic anisotropy energy (MAE) [20,27], and Curie temperature ( $T_c$ ) are two important parameters for the practical application of spintronic devices. At present, it is still impossible to calculate  $T_c$  directly from first-principles methods, and one has to rely on certain approximate schemes to obtain quantitative predictions from theory [28]. The  $T_c$  of the crystal system can be estimated within the framework of Mean Field Approximation (MFA) [29], which is often prioritized because it can be easily calculated using a simplified formula. However, it is well known that MFA overestimates the value of the  $T_c$  due to the inaccuracy in the

\* Corresponding authors.

E-mail addresses: [qiang.li@seu.edu.cn](mailto:qiang.li@seu.edu.cn) (Q. Li), [jlwang@seu.edu.cn](mailto:jlwang@seu.edu.cn) (J. Wang).

consideration of the correlations between spins. Therefore, the Monte Carlo method has been favored by its description of correlations between spins. The Ising model of some previous studies was used and discussed in extensive material predictions [30–34]. Nevertheless, it is widely accepted that the Ising model overestimate  $T_c$  as well since infinite MAE is assumed [30]. For example,  $T_c$  of monolayer CrCl<sub>3</sub> (66 K), CrBr<sub>3</sub> (86 K), and CrI<sub>3</sub> (107 K) [35] based on Ising mode is much higher than their measured values (17 K for CrCl<sub>3</sub>, 34 K for CrBr<sub>3</sub>, and 45 K for CrI<sub>3</sub>) [2,6,36]. Besides, the approximation of the Ising model is rather simplified, it contains only two spin states under extreme conditions, which greatly increases the difficulty of spin flipping.

Alternatively, the classical Heisenberg model changes the spin in the Ising model from a numerical value to a vector [24], the flip of the spin is no longer discrete but continuous, which can largely improve the Ising model. Therein, the Metropolis Monte Carlo (MMC) methods are employed to estimate the thermal averages of magnetic systems with classic Heisenberg model [24,25,37], several algorithms for spin changes have been proposed [38,39]. Yet, the MMC requires tremendous steps of generating new spin states to reach the thermal equilibrium and then take reasonable samplings, efficient approaches are still highly required. In this work, the concept of Euler angles and Quaternion is introduced to the MMC simulations, a program called SEU-mtc is compiled for both Ising and Heisenberg models. The program provides a universal framework for magnetic systems of both finite clusters and periodic structures, inputs only require the information of geometry,  $J$  values and MAE. The methods are tested for validation with theoretical numerical values and a case example of CrI<sub>3</sub> monolayer. The proposed methods will be available for use in open-source software package as soon as the manuscript is online.

## 2. Models and methods

### 2.1. Monte Carlo method

The simulation of phase transitions of magnetic systems is generally based on two models, the Ising model [40], and the classical Heisenberg model [41]. The Hamiltonian of the Ising model can be written in the form,

$$H = -J_1 \sum_{\langle i,j \rangle} \vec{s}_i^z \vec{s}_j^z - J_2 \sum_{\langle i,k \rangle} \vec{s}_i^z \vec{s}_k^z \dots \quad (1)$$

and the Hamiltonian of the classical Heisenberg model can be written in the form,

$$H = -J_1 \sum_{\langle i,j \rangle} \vec{s}_i \cdot \vec{s}_j - J_2 \sum_{\langle i,k \rangle} \vec{s}_i \cdot \vec{s}_k \dots - \sum_i A_i^z \vec{s}_i^z \vec{s}_i^z - \sum_i A_i^x \vec{s}_i^x \vec{s}_i^x \dots \quad (2)$$

where  $J_n$  is the exchange parameter, for example,  $J_1$  and  $J_2$  represent the nearest-neighbor exchange parameter and the next-nearest-neighbor exchange parameter,  $A_i^z$  is the MAE parameter for the magnetic axis in the z-axis,  $\vec{s}_i$  and  $\vec{s}_j$  are the vectors on a unit cell site.

For the systems that only consider the nearest-neighbor and the next-nearest-neighbor situation, and the easy-to-magnetic axis is clearly in the z-axis, the Hamiltonian can be written in this form,

$$H = -J_1 \sum_{\langle i,j \rangle} \vec{s}_i \cdot \vec{s}_j - J_2 \sum_{\langle i,k \rangle} \vec{s}_i \cdot \vec{s}_k - \sum_i A_i^z \vec{s}_i^z \vec{s}_i^z \quad (3)$$

Based on the Mermin–Wagner theorem, magnetic order is strongly suppressed by strong thermal fluctuations in the 2D isotropic Heisenberg model at finite temperatures [11]. However, this restriction be counteracted by magnetic anisotropy (MA), which is fundamentally critical to give rise to long-range magnetic ordering in 2D materials. Therefore, the 2D classic Heisenberg model with MAE can also have a non-zero Curie temperature in theory.

In this work, we assume that  $\vec{s} = \frac{1}{2}\vec{M}$  and the basic structure of the

grid is  $\{x, y, z, i\}$ . When the simulation is performed, the original cell is expanded into supercells and  $\{x, y, z\}$  are the index of the original cell in the supercell. As the supercell retains as a periodic structure, it should be chosen as large as possible to ensure the diversity and validity of the simulation, similar to the simulations of periodic molecular dynamics. Since computer performance and time are limited, it is necessary to select a suitable supercell size and improve computational efficiency. When the simulation is initiated, a random vector is randomly selected from the grid and generates a new trial vector to replace it, and the energy difference  $\Delta E = E_{new} - E_{init}$  with the new vector is calculated. Then the parameter  $p = \exp(-\Delta E/(k_B T))$  is computed as the probability of accepting this trial vector. When  $\Delta E < 0$ , the ratio  $p$  is greater than 1, indicating the trial vector could replace the initially selected vector [42]. If the trial vector is not accepted, the initially selected vector will not be changed. Therefore, the probability ratio can be written in this form,

$$p = \begin{cases} \exp\left(-\frac{\Delta E}{k_B T}\right), & \text{when } \Delta E > 0 \\ 1, & \text{when } \Delta E < 0 \end{cases} \quad (4)$$

The main part of the Metropolis Monte Carlo simulation is to repeat the above steps until the system reaches an equilibrium state and then continues to repeat several loops to collect the statistics observables (Fig. 1). Internal energy can be invoked as a criterion for determining the equilibrium state. In this work, four observations will be collected [43], the internal energy  $E$ , the magnetic moment  $M$ , the specific heat capacity  $C$ , and the magnetic susceptibility  $\chi$  as defined below.

$$E = \langle E \rangle = \frac{1}{N} \sum_i H_i \quad (5)$$

$$M = \langle \vec{M} \rangle = \frac{1}{N} \left| \sum_i \vec{M}_i \right| \quad (6)$$

$$C = \frac{\partial E}{\partial T} = \frac{(\Delta E)^2}{k_B T} = \frac{\langle E^2 \rangle - \langle E \rangle^2}{k_B T^2} \quad (7)$$

$$\chi = \frac{\partial M}{\partial T} = \frac{(\Delta \vec{M})^2}{k_B T} = \frac{\langle \vec{M}^2 \rangle - \langle \vec{M} \rangle^2}{k_B T} \quad (8)$$

### 2.2. Spin update

MMC simulation requires continuous spin updates and a mass of Monte Carlo steps (MCS) to reach a state within the thermal equilibrium. The trial spin states in the Markov chain [43] can be generated by trial moves from a given state to a random position on the spherical surface, which includes all the spin orientations (Fig. 2). Hinze and Nowak applied a combinational approach for efficient sampling of all available phase space, including small trial step (STS), uniform trial step (UTS), and reflection trial step (RTS), while the three independent approaches suit for systems at different temperatures [38]. Alzate-Cardona et al. proposed an adaptive Gaussian move to maintain the acceptance rate close to 50%, maximizing the calculation efficiency of phase space sampling [39]. In order to have a unified framework for all temperatures and uniform static distributions of the sphere points, the dynamic scheme with respect to the width of a cone around the initial spin orientation (step width  $\xi$ ) is adopted in this study (Scheme 1, left side). Specifically, an initial step width  $\xi$  of 1.0 is set and the Monte Carlo process with a limited number of steps (around 100 MCS) is pre-run for testing. In general, the  $\xi$  of 1.0, corresponding to a uniform trial step, would result in a low acceptance rate except for systems with high disorder. In that case, another pre-run will be performed for testing with a reduced  $\xi$  until the acceptance rate close to or slightly greater than 50% (Fig. 2). Subsequently, different  $\xi$  are used in different

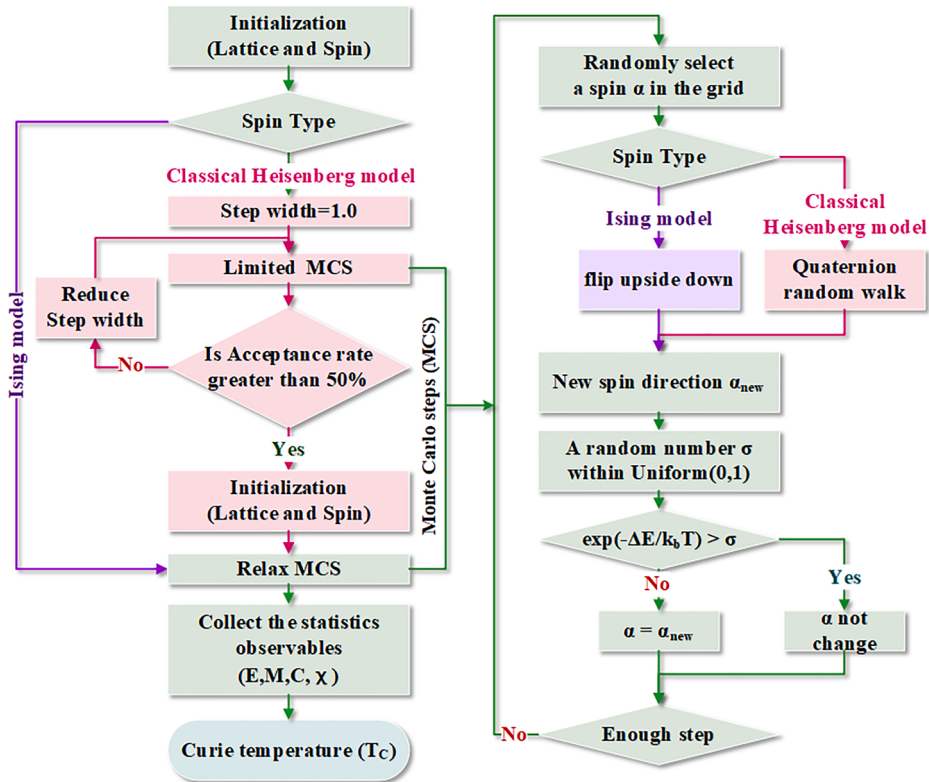


**Fig. 1.** Basic flow of the Metropolis Monte Carlo simulation method and the details of the Monte Carlo step loop.

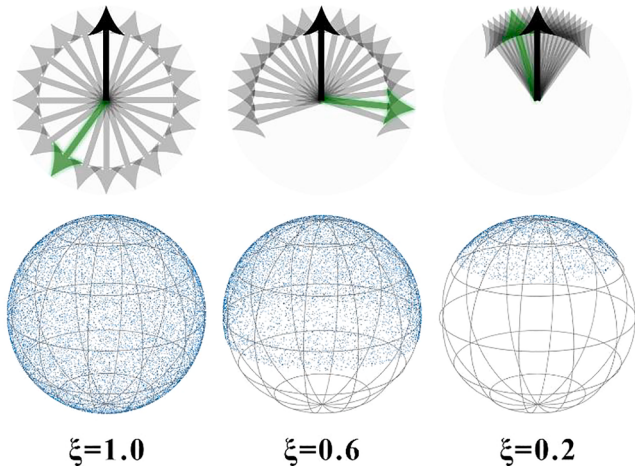


**Fig. 2.** Schematic and three-dimensional statistical distribution. arbitrarily step widths could be simulated. Large step widths are used at temperatures above Curie Temperature and narrow step widths are used at temperatures below Curie Temperature, which determined by preprocessing experiments to improve the simulation efficiency.

temperatures, making the microstructure have enough structural changes at different temperatures.

### 2.3. Concept of Euler angles and quaternion

The spin update process can be seen as random walks (RW) on the surface of the sphere. In fact, the random walk in the MMC can be treated as a rotation process as seen in the 3D rotation group (often denoted SO(3)). Therein Euler angles and quaternion, which are the most commonly used methods for description structures in 3D rendering

software [44–46], can provide an efficient solution. Taking advantage of the Euler angle, spin updates can be easily operated by a rotation matrix  $R$ . The coordinates of the spin states, both sphere and Cartesian coordinate, after each spin update can be obtained and stored in the meantime. Benefiting from the concise definition and converting function, quaternions avoid using the trigonometric function and thus save runtime memory consumption and reduce computation time. Furthermore, the quaternion and Euler angles can be converted to each other directly, which are beneficial to later framework conversion [47].

In the framework of Euler angles, referring to Tait-Bryan Euler angles [x-y-z] specifically, the rotation matrix is represented in the complete expression by Formula S1.

$$R = R_z(\gamma)R_y(\beta)R_x(\alpha) \quad (9)$$

In an intuitive presentation of the airplane rotation shown in Fig. 3 (a), the direction of the airplane can be modulated by corresponding yaw, pitch, and roll of the rotation matrix. In the case of a constant magnetic moment, the spin vector is rotated on a spherical surface with a fixed radius, *i.e.*, the length  $r$  is fixed. Analogous to airplane navigation, the direction of navigation is a matter of concern, but the attitude of the aircraft is irrelevant. Then the rotation matrix could be reduced to Formula S2:

$$R = R_z(\gamma)R_y(\beta)I \quad (10)$$

where  $I$  denote for the identity matrix in linear algebra.

Considering a spin update from place 1 to 3 in a Cartesian coordinate shown in Fig. 3(b), the rotation process can be accomplished by two rotational operations in the spherical coordinate, rotating  $\theta$  degrees on the  $y$ -axis and  $\varphi$  degrees on the  $z$ -axis. Consequently,  $\theta$  and  $\varphi$  can take place of  $\beta$  and  $\gamma$ , the Euler angles can be linked with sphere and Cartesian coordinates for further rotation processes.

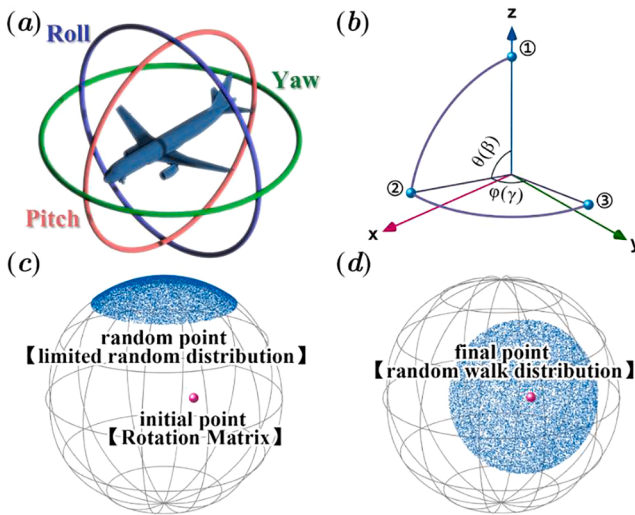


**Fig. 3.** (a) Schematic of yaw, pitch, and roll in the airplane principal axes. (b) The connection of spherical coordinates and rotation matrix of Euler angles. (c-d) The logic of the random walk with a given  $\xi$ . The left figure shows the initialization process of a random walk, which needs a random point and an initial point. The right figure shows the final situation after the rotation.

$$R = R_z(\varphi)R_y(\theta) = \begin{bmatrix} \cos(\theta)\cos(\varphi) & -\sin(\varphi) & \sin(\theta)\cos(\varphi) \\ \cos(\theta)\sin(\varphi) & \cos(\varphi) & \sin(\theta)\sin(\varphi) \\ -\sin(\theta) & 0 & \cos(\theta) \end{bmatrix} \quad (11)$$

According to Eqs. (9) and (11), the rotation matrix is a  $3 \times 3$  orthogonal matrix with determinant 1, which is determined by  $\theta$  and  $\varphi$  in this case. Due to the connection between the nine matrix elements, the rotation matrix can be simplified by quaternion method, which is developed by W. R. Hamilton in 1843 [48].

$$\begin{aligned} R_z(\varphi)R_y(\theta) &\Leftrightarrow \begin{pmatrix} q_x \\ q_y \\ q_z \\ q_w \end{pmatrix} = \begin{pmatrix} 0 \\ \sin(\theta/2) \\ 0 \\ \cos(\theta/2) \end{pmatrix} \cdot \begin{pmatrix} 0 \\ 0 \\ \sin(\varphi/2) \\ \cos(\varphi/2) \end{pmatrix} \\ &= \begin{pmatrix} \sin(\theta/2) \cdot \sin(\varphi/2) \\ \sin(\theta/2) \cdot \cos(\varphi/2) \\ \cos(\theta/2) \cdot \sin(\varphi/2) \\ \cos(\theta/2) \cdot \cos(\varphi/2) \end{pmatrix} \end{aligned} \quad (12)$$

In a routine procedure of MMC, the random walk process for spin updates starts with the generation of uniform distribution of possible spin orientations around a random selected spin state. With the help of Euler angles, a cone-like distribution can be first formed and then rotate to the position that the selected point is in the center of the cone. For instance, Fig. 3(c) shows that a random point (denoted as  $[x_\Delta, y_\Delta, z_\Delta]^T$ ) locates at an arbitrary place of a uniform distribution ( $\xi = 0.15$ ) at the north pole of the sphere. The rotation matrix calculated by the definition of the Euler angles.

$$R = R_z(\varphi_i)R_y(\theta_i) \quad (13)$$

Finally, the required points are obtained, and to improve the computational efficiency of the rotation matrix, the spherical coordinates for each calculation result are necessary to be recorded.

$$\begin{bmatrix} x \\ y \\ z \end{bmatrix} = R \cdot \begin{bmatrix} x_\Delta \\ y_\Delta \\ z_\Delta \end{bmatrix} \quad (14)$$

$$\theta = \arccos(z) \quad \text{and} \quad \varphi = \arctan2(y/x) \quad (15)$$

In addition, the previous step of rotating through the rotation matrix can be replaced by the product of quaternions [49]. And the complete expression is stored in Formula S3.

$$q_{new} = q_\Delta \cdot q_i \quad (16)$$

The rotation matrix and quaternion on the sphere can be converted to each other, which is also the original intention of the quaternion design. The relationship between the quaternion and the Cartesian coordinates can be obtained by converting the quaternion (Eq. (12)) into a rotation matrix (Eq. (11)) and converting the rotation matrix to Cartesian coordinates.

$$R(q_{new}) = \begin{bmatrix} 1 - 2q_y^2 - 2q_z^2 & -2q_xq_y - 2q_zq_w & 2q_yq_w - 2q_xq_z \\ 2q_zq_w - 2q_xq_y & 1 - 2q_x^2 - 2q_z^2 & 2q_yq_z + 2q_xq_w \\ -2q_xq_z - 2q_zq_w & 0 & 1 - 2q_x^2 - 2q_y^2 \end{bmatrix} \quad (17)$$

$$\begin{bmatrix} x \\ y \\ z \end{bmatrix} = R(q_{new}) \cdot \begin{bmatrix} 0 \\ 0 \\ 1 \end{bmatrix} = \begin{bmatrix} 2q_yq_w - 2q_xq_z \\ 2q_yq_z + 2q_xq_w \\ 1 - 2q_x^2 - 2q_y^2 \end{bmatrix} \quad (18)$$

## 2.4. Hysteresis loop

The external magnetic field is an important consideration when considering deviceization and the Hamiltonian of the classical Heisenberg model can be written in the form [50,51],

$$H = -J_1 \sum_{(i,j)} \vec{s}_i \cdot \vec{s}_j \cdots - \sum_i A_i^z \vec{s}_i^z \vec{s}_i^z \cdots - g\mu_B \vec{h} \sum_i \vec{s}_i \quad (19)$$

where  $g$  is the gyromagnetic ratio and  $\mu_B$  is the Bohr magneton. For convenience, in this work  $g\mu_B$  is set to 1 and you can scale the horizontal coordinate of the data later. Then Hamiltonian can be rewritten in this way,

$$H = -J_1 \sum_{(i,j)} \vec{s}_i \cdot \vec{s}_j \cdots - \sum_i A_i^z \vec{s}_i^z \vec{s}_i^z \cdots - \vec{h} \sum_i \vec{s}_i \quad (20)$$

In this case, not only the mode length of the magnetic moment but also the orientation of the magnetic moment needs to be recorded. Therefore, the statistical expression of the magnetic moment needs to be modified as follows.

$$M = \langle \vec{M} \rangle = \frac{1}{N} \sum_i \vec{M}_i \quad (21)$$

## 3. Result and discussion

### 3.1. Statistical distribution

Initializing a specific state is the first step of MMC. The ferromagnetic state is well-ordered and can be generated by all the vector pointing to the  $z$ -axis direction at the same time. As for a paramagnetic state, the disordered alignments are characterized. Essentially, subsequent MCS are all based on the random samplings of initiation microstructures, which covers all the possibilities. Therefore, a reasonable statistical distribution on the spherical surface plays a key role in MMC for the classical Heisenberg model. There have been numerous studies about the statistical distribution on the spherical surface in the early years, and several spherical surface random points generators (SRG) have been proposed [52–54]. Depending on the coordinates applied, these proposed methods in the literature can be divided into two categories, the spherical and Cartesian coordinates based methods.

#### 3.1.1. Spherical coordinate

SRG-1. Generate  $\theta$  and  $\varphi$  independent from the uniform distribution on  $[0, \pi]$  and  $[0, 2\pi]$ .

$$\begin{bmatrix} x \\ y \\ z \end{bmatrix} = \begin{bmatrix} \sin(\theta) \cdot \cos(\varphi) \\ \sin(\theta) \cdot \sin(\varphi) \\ \cos(\theta) \end{bmatrix} \quad (22)$$

**SRG-2.** Generate  $z$  and  $\varphi$  independent from uniform distribution on  $[-1, 1]$  and  $[0, 2\pi]$ .

$$\begin{bmatrix} \sin(\arccos(z)) \cdot \cos(\varphi) \\ \sin(\arccos(z)) \cdot \sin(\varphi) \\ z \end{bmatrix} \quad (23)$$

SRG-1 is constructed on the basis of uniform distribution of  $\theta$  and  $\varphi$  of the spherical coordinates and then converted to Cartesian coordinates. However, like the geographic coordinate system, the distribution of the meridians at the equator and the poles are quite distinct, and the meridians of the two poles are especially dense (Fig. 4(a)). When SRG-1 replacing  $\theta$  by  $\cos(\theta) \equiv z$ , which is inspired by the idea of the differential element of solid angle, is denoted as SRG-2 [55]. From Fig. 4(b), the uniform distribution of the spherical surface is obtained, but the time cost is increased along with the correction due to the utilization of inverse trigonometric functions.

### 3.1.2. Cartesian coordinate

**SRG-3.** Generate  $x_0, x_1, x_2$  from a uniform distribution on  $(-1, 1)$  and  $\text{norm} = \sqrt{x_0^2 + x_1^2 + x_2^2}$ .

$$\begin{bmatrix} x_0/\text{norm} \\ x_1/\text{norm} \\ x_2/\text{norm} \end{bmatrix} \quad (24)$$

**SRG-4.** Generate  $x_0, x_1, x_2$  from a normal distribution on  $(-1, 1)$  and  $\text{norm} = \sqrt{x_0^2 + x_1^2 + x_2^2}$  [54]. (Vector same as Eq. 24)

**SRG-5.** Generate  $x_0, x_1, x_2$  from a uniform distribution on  $(-1, 1)$

and  $\text{norm} = \sqrt{x_0^2 + x_1^2 + x_2^2}$ . Reject the group if  $\text{norm} \geq 1$ , and regenerate until a group  $x_0, x_1, x_2$  is obtained satisfying  $\text{norm} < 1$  (Vector same as Eq. 24) [52].

**SRG-6.** Generate  $x_0, x_1, x_2, x_3$  from a uniform distribution on  $(-1, 1)$  and  $r = x_0^2 + x_1^2 + x_2^2 + x_3^2$ . Reject the group if  $r \geq 1$ , and regenerate until a group  $x_0, x_1, x_2, x_3$  is obtained satisfying  $r < 1$  [52].

$$\begin{bmatrix} 2(x_1x_3 + x_0x_2)/r \\ 2(x_2x_3 - x_0x_1)/r \\ (x_0^2 + x_3^2 - x_1^2 - x_2^2)/r \end{bmatrix} \quad (25)$$

**SRG-7.** Generate  $x_0, x_1$  from a uniform distribution on  $(-1, 1)$  and  $r = x_0^2 + x_1^2$ . Reject the group if  $r \geq 1$ , and regenerate until a group  $x_0, x_1$  is obtained satisfying  $r < 1$  [52].

$$\begin{bmatrix} 2x_0\sqrt{1-r} \\ 2x_1\sqrt{1-r} \\ 1-2r \end{bmatrix} \quad (26)$$

SRG-3 crudely tilings the distribution of the cubes onto the surface of the sphere, resulting in eight aggregations that are displayed in Fig. 4(a) and Fig. S1. There are two ways to correct it based on SRG-3. The first way is to use a normal distribution method to replace uniform distribution, which is specifically expressed as SRG-4; the other way is to constrain all the points inside a sphere shape by threshold evaluation  $r < 1$ , then tiling it onto the surface of the sphere, which is specifically expressed as SRG-5. Alternative approaches including such valid value loops, SRG-6 and SRG-7, can also obtain uniform distribution. It should be noted that SRG-5, 6, and 7 have different dimensions, corresponding to three, four, and two dimensions, respectively. The variation of dimensions leads to different volume ratios: the volume ratio (area ratio) of the two-dimension is  $\frac{\pi R^2}{(2R)^2} = \frac{\pi}{4} = 0.785$ , three-dimension follows with

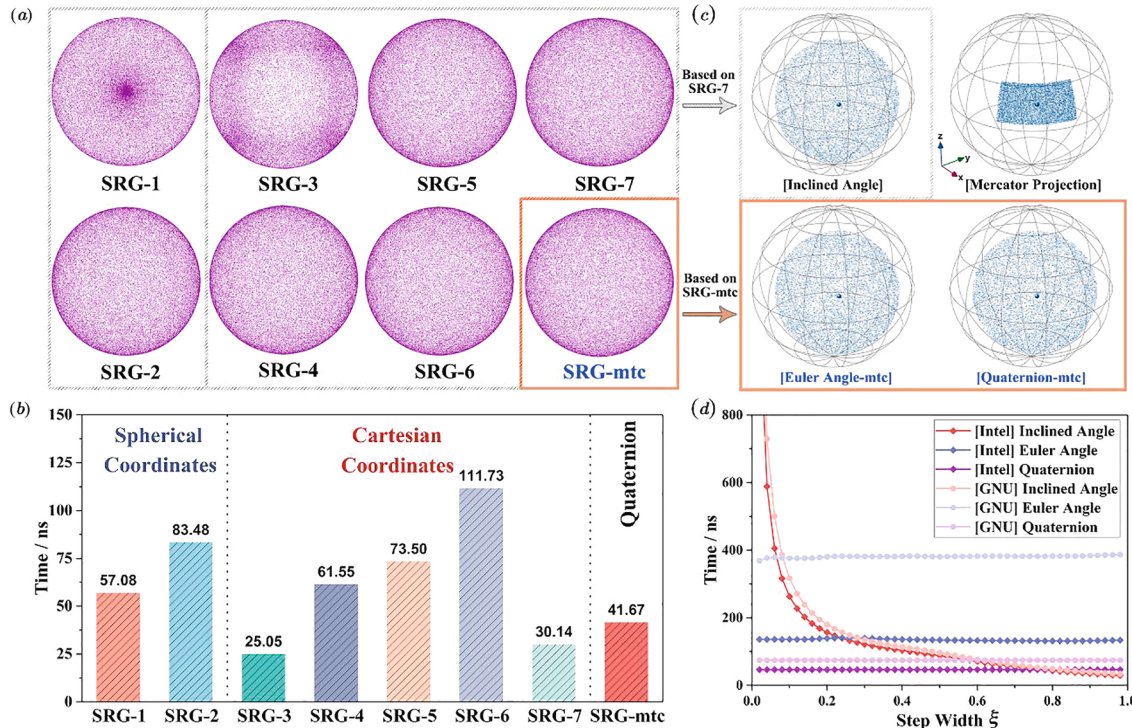


**Fig. 4.** (a) Statistical distribution of each method. Above distributions are all from the  $z$ -view, and more multiview projections are displayed in Fig. S1. (b) Relative performance of each method. The performance values are the average time of generating a random point on the spherical surface by intel compiler (lower is better). Specific values of each method by a different compiler are stored in Table S1. (c) The statistical distribution of each method with the same initial point. And the statistical distribution of each random walk methods with the same initial point in more extreme cases is stored in Fig. S2. (d) Relative performance of each valid random walk method in different step width  $\xi$ . The performance values are average time of generating a random point on the sphere surface around the initial point in different step width  $\xi$  (lower is better). Specific values of each valid random walk method in different step width  $\xi$  by a different compiler are stored in Table S2.

$$\frac{4\pi R^3/3}{(2R)^3} = \frac{\pi}{6} = 0.524, \text{ and four-dimension satisfies } \frac{\pi^2 R^4/2}{(2R)^4} = \frac{\pi^2}{25} = 0.308.$$

These ratios denote for the possibility that a trial vector is valid, i.e.  $r < 1$ , and large volume ratios mean high efficiency of the applied method. Therefore, a low-dimensional random number generator is more efficient for adoption comparing with generators with high-dimension.

### 3.1.3. Euler angles and quaternion

Comparing with Cartesian coordinate-based methods, the spherical coordinate benefits from facile rotations for the further random walk. According to SRG-2, a uniform statistical distribution is generated by replacing the  $\theta$  by  $\cos(\theta) \equiv z$ . And then the sampling of  $z$  and  $\varphi$  in the arbitrary range can lead to uniform distributions of the spherical surface. When the range of  $\theta$  is fixed and adjusting the range of  $z$  from an arbitrary number to 1, then a cone-like uniform distribution like Fig. 2 will be generated. The process can be incorporated into the definition of Euler angles by generating  $z_\Delta$  and  $\varphi_\Delta$  independent from uniform distributions on  $[1 - 2\xi, 1]$  and  $[0, 2\pi]$ .

$$\begin{bmatrix} x_\Delta \\ y_\Delta \\ z_\Delta \end{bmatrix} = R \begin{bmatrix} 0 \\ 0 \\ 1 \end{bmatrix} = \begin{bmatrix} \sin(\arccos(z_\Delta)) \cdot \cos(\varphi_\Delta) \\ \sin(\arccos(z_\Delta)) \cdot \sin(\varphi_\Delta) \\ z_\Delta \end{bmatrix} \quad (27)$$

The uniform distributions with given  $\theta$  and  $\varphi$  can also be converted into quaternion method form. Similar with Euler angles, generate  $z_\Delta$  and  $\varphi_\Delta$  independent from uniform distributions on  $[1 - 2\xi, 1]$  and  $[0, 2\pi]$ . Since the maximum range of  $\theta/2$  is in  $[0, \pi/2]$ , both the sine and cosine functions are positive. Hence this expression can reduce by inverse operation of double-angle formulas.

$$q_\Delta = \begin{pmatrix} \sqrt{(1-z_\Delta)/2} \cdot \sin(\varphi_\Delta/2) \\ \sqrt{(1-z_\Delta)/2} \cdot \cos(\varphi_\Delta/2) \\ \sqrt{(1+z_\Delta)/2} \cdot \sin(\varphi_\Delta/2) \\ \sqrt{(1+z_\Delta)/2} \cdot \cos(\varphi_\Delta/2) \end{pmatrix} \quad (28)$$

Here are some simple substitutions. Generate  $z_{\Delta 2}$  and  $\varphi_{\Delta 2}$  independent from uniform distributions on  $[0, \xi]$  and  $[0, \pi]$ . Substitute  $1 - 2z_{\Delta 2}$  for  $z_\Delta$  and  $2\varphi_{\Delta 2}$  for  $\varphi_\Delta$ . When  $\xi$  is equal to 1, a uniform distribution all over the spherical surface will be generated.

$$q_\Delta = \begin{pmatrix} \sqrt{z_{\Delta 2}} \cdot \sin(\varphi_{\Delta 2}) \\ \sqrt{z_{\Delta 2}} \cdot \cos(\varphi_{\Delta 2}) \\ \sqrt{1-z_{\Delta 2}} \cdot \sin(\varphi_{\Delta 2}) \\ \sqrt{1-z_{\Delta 2}} \cdot \cos(\varphi_{\Delta 2}) \end{pmatrix} \quad (29)$$

**SRG-mtc.** Generate  $z_2$  and  $\varphi_2$  independent from the uniform distribution on  $[0, 1]$  and  $[0, \pi]$ .

$$\begin{pmatrix} q_x \\ q_y \\ q_z \\ q_w \end{pmatrix} = \begin{pmatrix} \sqrt{z_2} \cdot \sin(\varphi_2) \\ \sqrt{z_2} \cdot \cos(\varphi_2) \\ \sqrt{1-z_2} \cdot \sin(\varphi_2) \\ \sqrt{1-z_2} \cdot \cos(\varphi_2) \end{pmatrix} \quad (30)$$

$$\begin{bmatrix} 2q_y q_w - 2q_x q_z \\ 2q_y q_z + 2q_x q_w \\ 1 - 2q_x^2 - 2q_y^2 \end{bmatrix} \quad (31)$$

Taking the advantage of Euler angles and quaternion, as we discussed in Sec. 2.3, we propose an alternative approach for statistical distribution. As shown in Fig. 4(b), SRG-mtc presents a uniform distribution on a spherical surface and is the second-best approach (slightly higher than SRG-7) among all the above-mentioned methods in terms of time efficiency. However, the Cartesian based methods, including SRG 4–7, suffer from low efficiency in the random walk, due to lack of the correlation between the rotation and Cartesian coordinate. In this respect, the SRG-mtc is proven to be an accurate and efficient approach for overall MMC simulations, which will be further shown in the Sec. 3.2.

### 3.2. Spherical surface random walk

The spin update, i.e., the spherical surface random walk plays an essential role in MCS, it determines the accuracy and efficiency of the whole simulation. For the Ising model, the orientation of the spin can only be positive or negative, thus the random walk for the Ising model corresponds to the flip of the spin direction. However, the spin of classical Heisenberg model is a vector that can point to arbitrarily direction, which is clearly distinct from the Ising model [41]. In this section, we introduce several approaches for random walk based on the corresponding statistical distribution methods as discussed above.

**RW-1** [Mercator Projection, based on SRG-1]. Generate  $\theta_\Delta$  and  $\varphi_\Delta$  independent from uniform distributions on  $[-\pi/2, \pi/2]$  and  $[-\pi, \pi]$ .

$$\theta = \theta_i + \theta_\Delta \cdot \xi \quad (32)$$

$$\varphi = \varphi_i + \varphi_\Delta \cdot \xi \quad (33)$$

Updating the spin by uniform perturbation of  $\theta$  and  $\varphi$  is a common misuse of spherical coordinate. Like cylindrical projections of the earth, the method makes high latitudes areas excessively distorted, leading to the fact the spin gets rid of two poles much more difficult than spin located at the equator, which will affect the validity of the trajectory of microstructures.

**RW-2** [Inclined Angle, based on SRG-7]. Generate a new random point in the spherical surface until the inclined angle between the initial point less than the step width  $\xi$ .

$$\text{until } \left( \vec{r}_{try} \cdot \vec{r}_i = \cos(\theta) > 1 - 2\xi \right) \text{ then } \vec{r} = \vec{r}_{try} \quad (34)$$

The Inclined angle method based on SRG-7 is exceedingly unstable for different step widths as we see from Fig. 4(d). When the temperature is higher than the transition temperature, the microstructure of the material exhibits a disordered state, which corresponds to a large step width situation. Therefore, the calculation at this time is especially efficient. However, in the case of low temperature (for most cases), the microstructure of the material exhibits a small perturbation phenomenon, which corresponds to a sharp step width situation. As a result, the calculation at this time is especially slow. When encountering novel materials, it is common to scan the relevant observations from low temperatures until the transition temperature is found. Consequently, the efficiency at low temperature, which corresponds to a sharp step width situation, plays a decisive role in MCS.

**RW-3** [Euler Angle, SRG-mtc]. Generate  $z_\Delta$  and  $\varphi_\Delta$  independent from uniform distributions on  $[1 - 2\xi, 1]$  and  $[0, 2\pi]$ . Then using rotation matrix to transform the random point to a new point around the initial point [46,56–58]. For convenience, basic information should not only save cartesian coordinates ( $x, y, z$ ) but also save the spherical coordinate( $\theta, \varphi$ ). The corresponding equation detailed expansion will be shown in Formula S4.

$$\begin{bmatrix} x_\Delta \\ y_\Delta \\ z_\Delta \end{bmatrix} = \begin{bmatrix} \sin(\arccos(z_\Delta)) \cdot \cos(\varphi_\Delta) \\ \sin(\arccos(z_\Delta)) \cdot \sin(\varphi_\Delta) \\ z_\Delta \end{bmatrix} \quad (35)$$

$$\begin{bmatrix} x \\ y \\ z \end{bmatrix} = R_z(\varphi_i) R_y(\theta_i) \cdot \begin{bmatrix} x_\Delta \\ y_\Delta \\ z_\Delta \end{bmatrix} \quad (36)$$

$$\theta = \arccos(z) \text{ and } \varphi = \arctan2(y/x) \quad (37)$$

**RW-4** [Quaternion, SRG-mtc]. Generate  $z_{\Delta 2}$  and  $\varphi_{\Delta 2}$  independent from uniform distributions on  $[0, \xi]$  and  $[0, \pi]$ . Converting the restricted random quaternion to a new quaternion around the initial point [46,48,59,60]. For convenience, basic information should not only save cartesian coordinates ( $x, y, z$ ) but also save quaternion information  $(q_x, q_y, q_z, q_w)$ .

$$\begin{pmatrix} q_{\Delta x} \\ q_{\Delta y} \\ q_{\Delta z} \\ q_{\Delta w} \end{pmatrix} = \begin{pmatrix} \sqrt{z_{\Delta 2}} \cdot \sin(\varphi_{\Delta 2}) \\ \sqrt{z_{\Delta 2}} \cdot \cos(\varphi_{\Delta 2}) \\ \sqrt{1 - z_{\Delta 2}} \cdot \sin(\varphi_{\Delta 2}) \\ \sqrt{1 - z_{\Delta 2}} \cdot \cos(\varphi_{\Delta 2}) \end{pmatrix} \quad (38)$$

$$\begin{pmatrix} q_x \\ q_y \\ q_z \\ q_w \end{pmatrix} = \begin{pmatrix} q_{\Delta w} \cdot q_{ix} + q_{\Delta x} \cdot q_{iw} + q_{\Delta y} \cdot q_{iz} - q_{\Delta z} \cdot q_{iy} \\ q_{\Delta w} \cdot q_{iy} - q_{\Delta x} \cdot q_{iz} + q_{\Delta y} \cdot q_{iw} + q_{\Delta z} \cdot q_{ix} \\ q_{\Delta w} \cdot q_{iz} + q_{\Delta x} \cdot q_{iy} - q_{\Delta y} \cdot q_{ix} + q_{\Delta z} \cdot q_{iw} \\ q_{\Delta w} \cdot q_{iw} - q_{\Delta x} \cdot q_{ix} - q_{\Delta y} \cdot q_{iy} - q_{\Delta z} \cdot q_{iz} \end{pmatrix} \quad (39)$$

$$\begin{bmatrix} x \\ y \\ z \end{bmatrix} = \begin{bmatrix} 2q_y q_w + 2q_x q_z \\ 2q_y q_z + 2q_x q_w \\ 1 - 2q_x^2 - 2q_y^2 \end{bmatrix} \quad (40)$$

Euler angle and quaternion methods avoids the loop of valid value evaluation in RW-2, thus, these methods are not influenced by step width on the computing time accordingly. For high-performance computers, trigonometric operations are more expensive types compared to numerical operations. A benchmark about the performance of each basis mathematical operations is listed in Fig. S3 and Table S3. Based on the platform-optimized compiler, the average time required for the trigonometric operations is five times as much as that for the numerical operation. The Quaternion method is more complicated, and it needs to store more information than the Euler angle method. However, it is still high-efficiency in the calculation time since the quaternion method avoids using the trigonometric function as much as possible. Even based on the platform-optimized compiler, the quaternion method also has a three times performance improvement than the Euler angle method. In all, the quaternion based on SRG-mtc and intel compile presents the most stable and efficient one among all the methods considered.

### 3.3. Program

#### 3.3.1. Universal configuration

From Ising (Eq. (1)) and Heisenberg (Eq. (2)) models, the magnetic couplings can be simplified to cases that only the interactions from nearest neighbors are considered. However, the consideration of next-nearest neighbors or high orders is required to obtain reliable and accurate results for complex systems. In addition, the lattice modeling can also be quite different by the geometry structures and point groups of systems, including cubic, hexagonal, etc. Therefore, a universal configuration scheme is required for an easy-to-operate program. For the target SEU-mtc program, a list container called Configure card for each magnetic atom in the lattice, where each row in the list container holds information in three categories and five values, is proposed. As shown in Fig. 5(a), for a single magnetic atom in a simple cubic lattice, there are four nearest neighbors ( $J_1$ ) and four next-nearest neighbors ( $J_2$ ). The Configure card contains values in three categories, where  $J_{num}$  determines which exchange parameter will be used,  $Offset_{(x,y,z)}$  determines which cell in the supercell contains the neighbor atom and  $Atom_{index}$  determines which one is the neighbor atom. Another example of monolayer  $\text{CrI}_3$  is shown in Fig. 5(b), the system contains two magnetic atoms per cell, which can be correspondingly represented by two Configure cards. With the transformation by these cards, the configuration files like POSCAR can be read and recorded for further calculations. Then a module, which generates list containers by analyzing periodic structure files, can be consolidated into the program.

#### 3.3.2. Code design

The code is divided into three parts, the first part is the global setting module, where will contain macro definitions of global physical and mathematical related constants, random number generation and a fast math library. The second part is the file parsing module, which first parses the parameters of the input file and assigns values accordingly and determines whether to parse the crystal coordinates file POSCAR

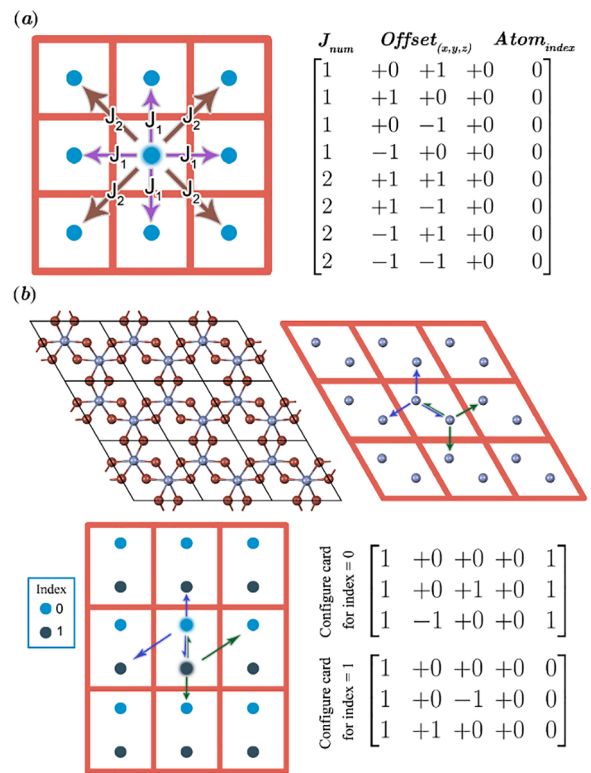


Fig. 5. (a) Schematic diagram and configure card of 2D simple cube lattice. In the current situation, only the nearest neighbors and the nearest neighbors are considered. (b) Schematic diagram and configure cards of monolayer  $\text{CrI}_3$  lattice. In this case, each cell has two magnetic atoms, but only the nearest neighbors are considered.

according to the input parameters. The third part is the simulation calculation module, in which the calculation simulation and corresponding parameters are established according to the configuration information and simulated in parallel. The program is based on the C++ language of the C++98 standard, and parallel simulation is performed by Message Passing Interface (MPI3).

### 3.4. Model validation and application

Next, the program is tested for validation with standard methods. The square lattice two-dimensional Ising model can be derived numerically by a theoretical derivation that  $k_B T/J_1 = 2/\log(\cot(\frac{\pi}{8})) \approx 2.269$  [61]. In consequence, the 2D Ising model could serve as a benchmark for checking the basic flow of the program, the detailed parameter setting and the input file of this program are displayed in the Config S1. Fig. 6(a) illustrates the change of the four main observables including the internal energy  $E$ , the magnetic moment  $M$ , the specific heat capacity  $C$ , and the magnetic susceptibility  $\chi$  with different grid sizes. Clearly, with the simulated grid size increases, the peaks, especially two second order phases transitions ( $C$  and  $\chi$ ), become sharper and closer to the theoretical value (dashed lines in Fig. 6(a)). For molecular dynamics, larger grids, which contain complex long-range relationships, are often required to describe the realistic situation while the computational costs grow rapidly in the meantime. In this simulation, the consequence of a grid size of  $100*100*1$  is proved to be large enough to approach the theoretical value (Fig. 6(a)).

Although the 2D Heisenberg model without MAE has the Mermin-Wagner theorem limitation, it is possible to benchmark the 3D Heisenberg model to evaluate the program. For instance, the numerical approximation expression derived from the high temperature expansion method is  $k_B T/J_1 \approx 1.44$  [62,63]. The specific parameter settings and

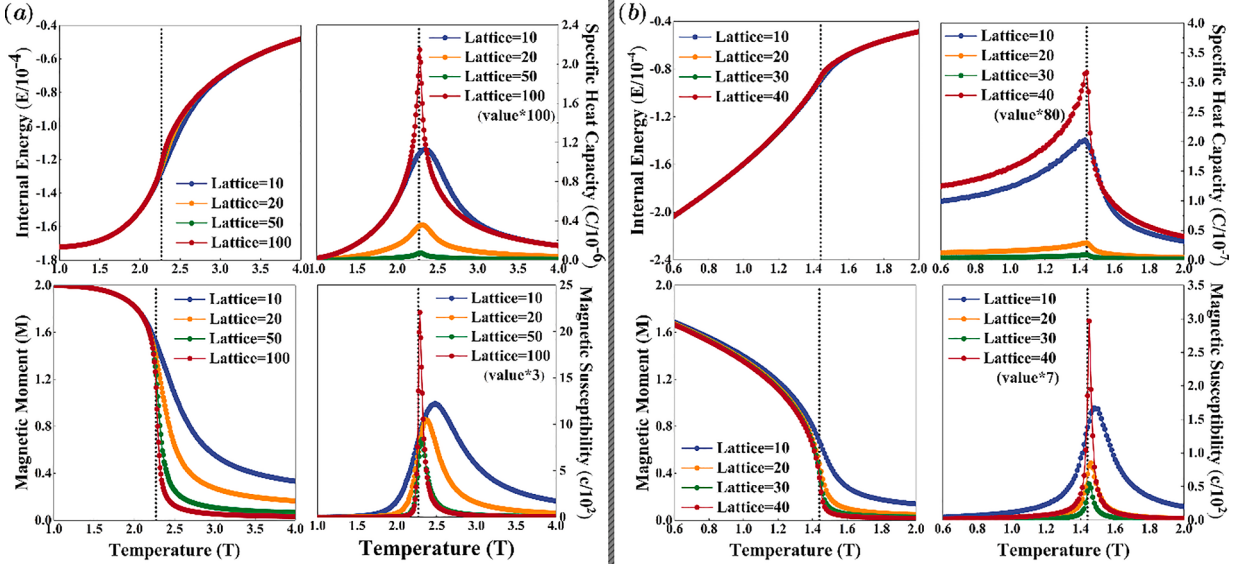


**Fig. 6.** (a) Internal energy  $E$ , specific heat capacity  $C$ , magnetic moment  $M$  and magnetic susceptibility  $\chi$  of 2D Ising model on a simple cubic lattice. The peak of heat capacities of large grids can be seen to be sharper and closer to the theoretical value than small grids. (b).  $E$ ,  $C$ ,  $M$ , and  $\chi$  of 3D Heisenberg model on a simple cubic lattice.

the input file of this program are displayed in the Config S2 and the simulated curves of the four observables are shown in Fig. 6(b). It is expectable that a rapid increase in computational time for the three-dimensional grid comparing with 2D cases, the consequence of  $40 \times 40 \times 40$  grid is then proved to be close to the numerical approximation expression of 3d Heisenberg model.

For an application example, we show the star 2D material of monolayer CrI<sub>3</sub> based on the previous theoretical calculations [35],

other examples can be found in previous reported references [24,35,64–66]. The specific consequence is shown in Fig. 7 and the explicit configuration parameters are stored in Config S3. As can be seen from Fig. 7(a), there is no obvious gradient change in internal energy  $E$  near the  $T_c$ , but the second-order phase transition variable, the specific heat capacity  $C$ , has a clear peak at the simulated  $T_c$ . Same as the relationship between  $E$  and  $C$ , the magnetic moment  $M$  and the magnetic susceptibility  $\chi$  also play an active role in searching the  $T_c$  (Fig. 7(b)).

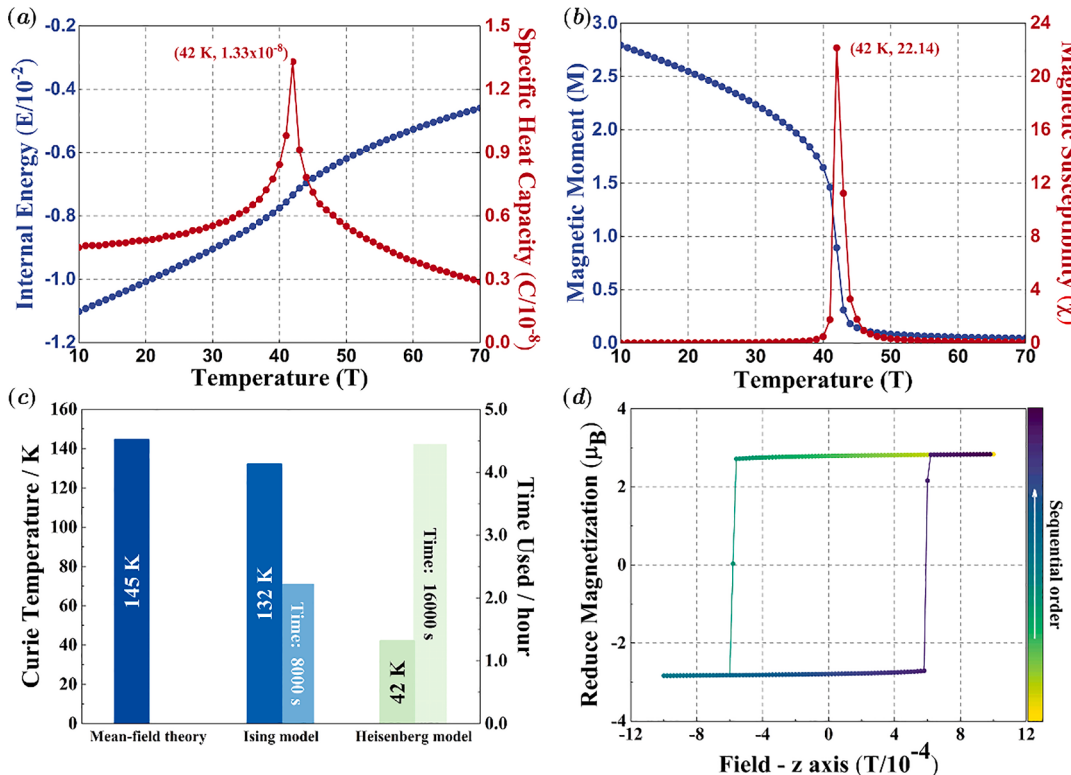


**Fig. 7.** (a) Internal energy  $E$  and specific heat capacity  $C$ , (b) magnetic moment  $M$  and magnetic susceptibility  $\chi$  of the 2D Heisenberg model of monolayer CrI<sub>3</sub>. The Curie transition temperature of the grid set to  $100 \times 100 \times 1$  of the Heisenberg model is much closer to the experimental measurement 45 K. (c) The calculated  $T_c$  and time cost by different methods. MMC methods all based on  $100 \times 100 \times 1$  lattice and repeat 10 times. (d) The hysteresis loop of CrI<sub>3</sub> at 10 K.

Consequently, a Curie temperature of 42 K is obtained with 100\*100\*1 grid size, the result agrees well with the experimental value of 45 K. On the contrary, methods with approximations including mean field theory and Ising model largely overestimate the  $T_c$  of 145.5 K and 132 K, respectively. The total wall time of a cycle simulation of the Heisenberg model is within half-hour (Fig. 7(c)), which is efficient even though the direct comparison with other methods is not performed since the detailed compilation of other methods is not available. Furthermore, the hysteresis loop of CrI<sub>3</sub>, which shows the relationship between the induced magnetic flux density and the magnetizing force, at 10 K is simulated as an application example of SER-mtc to learn more magnetic properties of the materials.

The SEU-mtc program can further provide a visualization scheme for the detailed information of the microstructures as shown in Fig. 8. For this purpose, SEU-mtc needs to save the geometry information from POSCAR and spin directions acting on atoms in XSF format (an internal XCrySDen structure format), which are used to describe forces.

#### 4. Conclusion

In summary, novel statistical distribution and spherical surface random walk algorithms based on Euler angle and quaternion that are borrowed from the ideas from 3D rendering are proposed, in which the quaternion method is proved to be particularly efficient in spin updates. The time efficiency can be also guaranteed by keeping the acceptance rate close to 50%, which is achieved by limited test runs with the variation of step width. The validation of the proposed methods is conducted by the comparison with the numerical approximations from both the 2D square lattice Ising model and the 3D cubic lattice Heisenberg model, showing excellent agreement in terms of the simulated quantities of internal energy, magnetic moment, specific heat capacity, and magnetic susceptibility. In addition, the methods are further evaluated by the simulation of the hotspot 2D magnetic material CrI<sub>3</sub> and a Curie transition temperature 42 K is obtained. The result is close to the experimental value of 45 K while the Ising model, on the contrary, largely overestimates the transition by 132 K. Then a universal framework for the magnetic Curie temperature simulation calculation tool called SEU-mtc is compiled. The program includes several distinct features. (1) Both Heisenberg model and Ising model can be simulated. (2) Neighbor relationship is determined by periodic coordinate information file like POSCAR of VASP input files, thus both periodic and finite cluster systems can be simulated. (3) Curie temperature simulation and Hysteresis loop simulation can be realized. (4) All the magnetic states with insight lattice microstructure can be instantaneously stored at different temperatures for visualization or other post-processing. (5) A universal configuration card scheme is proposed to store information to establish a universal simulation tool. The program reads the coordinate files of investigated systems with different symmetries and transfers the neighbor relationships into a separate table automatically for easy post-processing. The program is feasible and requires simple inputs including the information of geometry, exchange coupling constants and magnetic anisotropy energy.

#### 5. Data availability

All data used in this paper are available from the author upon request.

#### CRediT authorship contribution statement

**Yehui Zhang:** Software, Data curation, Investigation, Writing - original draft. **Bing Wang:** Methodology. **Yilv Guo:** Conceptualization, Methodology. **Qiang Li:** Supervision. **Jinlan Wang:** Supervision, Funding acquisition.

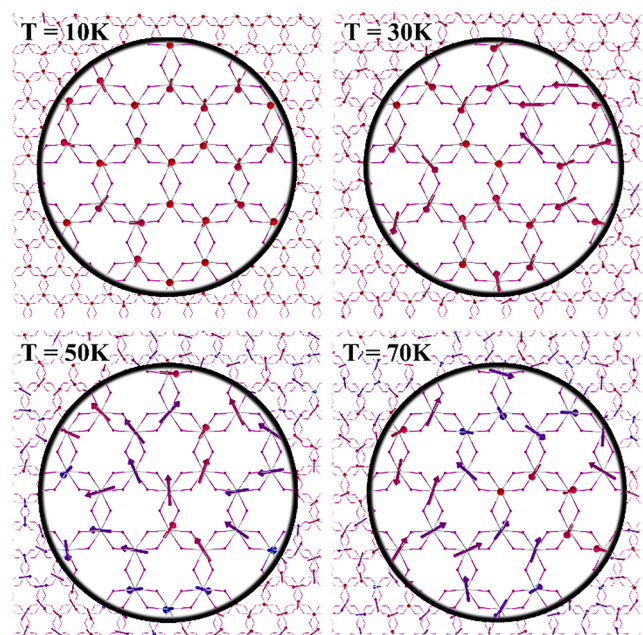


Fig. 8. Local information of 2D Heisenberg model of CrI<sub>3</sub> at different temperatures.

#### Declaration of Competing Interest

The authors declare that they have no known competing financial interests or personal relationships that could have appeared to influence the work reported in this paper.

#### Acknowledgements

This work is supported by the National Key R&D Program of China (Grant No. 2017YFA0204800), National Natural Science Foundation of China (Grant No. 21525311, 21703032, 12047517), and the Fundamental Research Funds for the Central Universities of China. The authors thank the computational resources from the Big Data Computing Center of Southeast University and National Supercomputing Center of Tianjin.

#### Appendix A. Supplementary data

Supplementary data to this article can be found online at <https://doi.org/10.1016/j.commatsci.2021.110638>.

#### References

- [1] B. Huang, G. Clark, E. Navarro-Moratalla, D.R. Klein, R. Cheng, K.L. Seyler, D. Zhong, E. Schmidgall, M.A. McGuire, D.H. Cobden, W. Yao, D.i. Xiao, P. Jarillo-Herrero, X. Xu, Layer-dependent ferromagnetism in a van der Waals crystal down to the monolayer limit, *Nature* 546 (7657) (2017) 270–273, <https://doi.org/10.1038/nature22391>.
- [2] C. Gong, L. Li, Z. Li, H. Ji, A. Stern, Y. Xia, T. Cao, W. Bao, C. Wang, Y. Wang, Z. Q. Qiu, R.J. Cava, S.G. Louie, J. Xia, X. Zhang, Discovery of intrinsic ferromagnetism in two-dimensional van der Waals crystals, *Nature* 546 (7657) (2017) 265–269, <https://doi.org/10.1038/nature22060>.
- [3] Y. Deng, Y. Yu, Y. Song, J. Zhang, N.Z. Wang, Z. Sun, Y. Yi, Y.Z. Wu, S. Wu, J. Zhu, J. Wang, X.H. Chen, Y. Zhang, Gate-tunable room-temperature ferromagnetism in two-dimensional Fe<sub>3</sub>GeTe<sub>2</sub>, *Nature* 563 (7729) (2018) 94–99, <https://doi.org/10.1038/s41586-018-0626-9>.
- [4] Z. Fei, B. Huang, P. Malinowski, W. Wang, T. Song, J. Sanchez, W. Yao, D.i. Xiao, X. Zhu, A.F. May, W. Wu, D.H. Cobden, J.-H. Chu, X. Xu, Two-dimensional itinerant ferromagnetism in atomically thin Fe<sub>3</sub>GeTe<sub>2</sub>, *Nat. Mater.* 17 (9) (2018) 778–782, <https://doi.org/10.1038/s41563-018-0149-7>.
- [5] X. Cai, T. Song, N.P. Wilson, G. Clark, M. He, X. Zhang, T. Taniguchi, K. Watanabe, W. Yao, D.i. Xiao, M.A. McGuire, D.H. Cobden, X. Xu, Atomically thin CrCl<sub>3</sub>: an in-plane layered antiferromagnetic insulator, *Nano Lett.* 19 (6) (2019) 3993–3998, <https://doi.org/10.1021/acs.nanolett.9b0131710.1021/acs.nanolett.9b01317.s001>.

- [6] H.H. Kim, B. Yang, S. Li, S. Jiang, C. Jin, Z. Tao, G. Nichols, F. Sfigakis, S. Zhong, C. Li, S. Tian, D.G. Cory, G.-X. Miao, J. Shan, K.F. Mak, H. Lei, K. Sun, L. Zhao, A. W. Tsen, Evolution of interlayer and intralayer magnetism in three atomically thin chromium trihalides, *Proc. Natl. Acad. Sci.* 116 (23) (2019) 11131–11136, <https://doi.org/10.1073/pnas.1902100116>.
- [7] H.L. Zhuang, Y. Xie, P.R.C. Kent, Computational discovery of ferromagnetic semiconducting single-layer CrSnTe<sub>3</sub>, *Phys. Rev. B* 92 (2015), 035407, <https://doi.org/10.1103/PhysRevB.92.035407>.
- [8] J. Zhou, Q. Sun, Magnetism of phthalocyanine-based organometallic single porous sheet, *J. Am. Chem. Soc.* 133 (38) (2011) 15113–15119, <https://doi.org/10.1021/ja204990j>.
- [9] X. Li, X. Wu, J. Yang, Room-temperature half-metallicity in La(Mn, Zn)AsO alloy via element substitutions, *J. Am. Chem. Soc.* 136 (15) (2014) 5664–5669, <https://doi.org/10.1021/ja412317s>.
- [10] J. Liu, Q. Sun, Enhanced ferromagnetism in a Mn<sub>3</sub>C<sub>12</sub>N<sub>12</sub>H<sub>12</sub> sheet, *ChemPhysChem* 16 (3) (2015) 614–620, <https://doi.org/10.1002/cphc.201402713>.
- [11] N.D. Mermin, H. Wagner, Absence of ferromagnetism or antiferromagnetism in one- or two-dimensional isotropic heisenberg models, *Phys. Rev. Lett.* 17 (22) (1966) 1133–1136, <https://doi.org/10.1103/PhysRevLett.17.1133>.
- [12] C. Gong, X. Zhang, Two-dimensional magnetic crystals and emergent heterostructure devices, *Science* 363 (6428) (2019) eaav4450, <https://doi.org/10.1126/science:aav4450>.
- [13] M. Kan, J. Zhou, Q. Sun, Y. Kawazoe, P. Jena, The intrinsic ferromagnetism in a MnO<sub>2</sub> monolayer, *J. Phys. Chem. Lett.* 4 (20) (2013) 3382–3386, <https://doi.org/10.1021/jz4017848>.
- [14] M. Ashton, D. Gluhovic, S.B. Sinnott, J. Guo, D.A. Stewart, R.G. Hennig, Two-dimensional intrinsic half-metals with large spin gaps, *Nano Lett.* 17 (9) (2017) 5251–5257, <https://doi.org/10.1021/acs.nanolett.7b01367>.
- [15] S. Zhang, R. Xu, W. Duan, X. Zou, Intrinsic half-metallicity in 2D ternary chalcogenides with high critical temperature and controllable magnetization direction, *Adv. Funct. Mater.* 29 (14) (2019) 1808380, <https://doi.org/10.1002/adfm.201808380>.
- [16] Y. Feng, X. Wu, G. Gao, High tunnel magnetoresistance based on 2D Dirac spin gapless semiconductor VCl<sub>3</sub>, *Appl. Phys. Lett.* 116 (2) (2020) 022402, <https://doi.org/10.1063/1.5128204>.
- [17] X. Li, J. Yang, Realizing two-dimensional magnetic semiconductors with enhanced curie temperature by antiaromatic ring based organometallic frameworks, *J. Am. Chem. Soc.* 141 (1) (2019) 109–112, <https://doi.org/10.1021/jacs.8b11346>.
- [18] C. Liu, S. Guan, H. Yin, W. Wan, Y. Wang, Y. Zhang, γ-GeSe: a two-dimensional ferroelectric material with doping-induced ferromagnetism, *Appl. Phys. Lett.* 115 (25) (2019) 252904, <https://doi.org/10.1063/1.5133022>.
- [19] H. Kumar, N.C. Frey, L. Dong, B. Anasori, Y. Gogotsi, V.B. Shenoy, Tunable magnetism and transport properties in nitride MXenes, *ACS Nano* 11 (8) (2017) 7648–7655, <https://doi.org/10.1021/acsnano.7b02578>.
- [20] B. Wang, X. Zhang, Y. Zhang, S. Yuan, Y. Guo, S. Dong, J. Wang, Prediction of a two-dimensional high-TC f-electron ferromagnetic semiconductor, *Mater. Horiz.* 7 (6) (2020) 1623–1630, <https://doi.org/10.1039/DOMH00183J>.
- [21] M. Bonilla, S. Kolekar, Y. Ma, H.C. Diaz, V. Kalappatil, R. Das, T. Eggers, H. R. Gutierrez, M.-H. Phan, M. Batzill, Strong room-temperature ferromagnetism in VSe<sub>2</sub> monolayers on van der Waals substrates, *Nat. Nanotechnol.* 13 (4) (2018) 289–293, <https://doi.org/10.1038/s41565-018-0063-9>.
- [22] Y. Ma, Y. Dai, M. Guo, C. Niu, Y. Zhu, B. Huang, Evidence of the existence of magnetism in pristine VX<sub>2</sub> monolayers (X = S, Se) and their strain-induced tunable magnetic properties, *ACS Nano* 6 (2) (2012) 1695–1701, <https://doi.org/10.1021/nm020467z>.
- [23] Z.-L. Liu, X.-L. Wu, Y. Shao, J. Qi, Y. Cao, L. Li, Huang, C. Liu, J.-O. Wang, Q.-J. Zheng, Z.-L. Zhu, K. Ibrahim, Y.-L. Wang, H.-J. Gao, Epitaxially grown monolayer VSe<sub>2</sub>: an air-stable magnetic two-dimensional material with low work function at edges, *Sci. Bull.* 63 (7) (2018) 419–425, <https://doi.org/10.1016/j.scib.2018.03.008>.
- [24] W.-B. Zhang, Q. Qu, P. Zhu, C.-H. Lam, Robust intrinsic ferromagnetism and half semiconductor in stable two-dimensional single-layer chromium trihalides, *J. Mater. Chem. C* 3 (48) (2015) 12457–12468, <https://doi.org/10.1039/C5TC02840J>.
- [25] X. Li, J. Yang, Cr<sub>x</sub>Te<sub>3</sub> (X = Si, Ge) nanosheets: two dimensional intrinsic ferromagnetic semiconductors, *J. Mater. Chem. C* 2 (34) (2014) 7071, <https://doi.org/10.1039/C4TC01193G>.
- [26] H.L. Zhuang, P.R.C. Kent, R.G. Hennig, Strong anisotropy and magnetostriction in the two-dimensional Stoner ferromagnet Fe<sub>3</sub>GeTe<sub>2</sub>, *Phys. Rev. B* 93 (2016), 134407, <https://doi.org/10.1103/PhysRevB.93.134407>.
- [27] B. Wang, Y. Zhang, L. Ma, Q. Wu, Y. Guo, X. Zhang, J. Wang, MnX (X = P, As) monolayers: a new type of two-dimensional intrinsic room temperature ferromagnetic half-metallic material with large magnetic anisotropy, *Nanoscale* 11 (10) (2019) 4204–4209, <https://doi.org/10.1039/C8NR09734H>.
- [28] T. Olsen, Theory and simulations of critical temperatures in CrI<sub>3</sub> and other 2D materials: easy-axis magnetic order and easy-plane Kosterlitz-Thouless transitions, *MRS Commun.* 9 (4) (2019) 1142–1150, <https://doi.org/10.1557/mrc.2019.117>.
- [29] Z. Liu, J. Liu, J. Zhao, YN<sub>2</sub> monolayer: novel p-state Dirac half metal for high-speed spintronics, *Nano Res.* 10 (6) (2017) 1972–1979, <https://doi.org/10.1007/s12274-016-1384-3>.
- [30] Y. Sun, Z. Zhuo, X. Wu, J. Yang, Room-temperature ferromagnetism in two-dimensional Fe<sub>2</sub>Si nanosheet with enhanced spin-polarization ratio, *Nano Lett.* 17 (5) (2017) 2771–2777, <https://doi.org/10.1021/acs.nanolett.6b04884>.
- [31] B. Wang, Q. Wu, Y. Zhang, Y. Guo, X. Zhang, Q. Zhou, S. Dong, J. Wang, High Curie-temperature intrinsic ferromagnetism and hole doping-induced half-metallicity in two-dimensional scandium chlorine monolayers, *Nanoscale Horiz.* 3 (5) (2018) 551–555, <https://doi.org/10.1039/C8NH00101D>.
- [32] X. Zhang, B. Wang, Y. Guo, Y. Zhang, Y. Chen, J. Wang, High Curie temperature and intrinsic ferromagnetic half-metallicity in two-dimensional Cr<sub>2</sub>X<sub>4</sub> (X = S, Se, Te) nanosheets, *Nanoscale Horiz.* 4 (4) (2019) 859–866, <https://doi.org/10.1039/C9NH00038K>.
- [33] J. He, S. Ma, P. Lyu, P. Nachtigall, Unusual Dirac half-metallicity with intrinsic ferromagnetism in vanadium trihalide monolayers, *J. Mater. Chem. C* 4 (13) (2016) 2518–2526, <https://doi.org/10.1039/C6TC00409A>.
- [34] T. Zhao, J. Zhou, Q. Wang, Y. Kawazoe, P. Jena, Ferromagnetic and half-metallic FeC<sub>2</sub> monolayer containing C<sub>2</sub> dimers, *ACS Appl. Mater. Interfaces.* 8 (39) (2016) 26207–26212, <https://doi.org/10.1021/acsami.6b07482>.
- [35] J. Liu, Q. Sun, Y. Kawazoe, P. Jena, Exfoliating biocompatible ferromagnetic Cr-trihalide monolayers, *Phys. Chem. Chem. Phys.* 18 (13) (2016) 8777–8784, <https://doi.org/10.1039/C5CP04835D>.
- [36] Z. Zhang, J. Shang, C. Jiang, A. Rasmussen, W. Gao, T. Yu, Direct photoluminescence probing of ferromagnetism in monolayer two-dimensional CrBr<sub>3</sub>, *Nano Lett.* 19 (5) (2019) 3138–3142, <https://doi.org/10.1021/acs.nanolett.9b00553>.
- [37] H.J. Xiang, S.-H. Wei, M.-H. Whangbo, Origin of the structural and magnetic anomalies of the layered compound SrFeO<sub>2</sub>: a density functional investigation, *Phys. Rev. Lett.* 100 (2008) 167207, <https://doi.org/10.1103/PhysRevLett.100.167207>.
- [38] D. Hinze, U. Nowak, Monte Carlo simulation of magnetization switching in a Heisenberg model for small ferromagnetic particles, *Comput. Phys. Commun.* 121–122 (1999) 334–337, [https://doi.org/10.1016/S0010-4655\(99\)00348-3](https://doi.org/10.1016/S0010-4655(99)00348-3).
- [39] J.D. Alzate-Cardon, D. Sabogal-Suárez, R.F.L. Evans, E. Restrepo-Parras, Optimal phase space sampling for Monte Carlo simulations of Heisenberg spin systems, *J. Phys. Condens. Matter.* 31 (9) (2019) 095802, <https://doi.org/10.1088/1361-648X/aaef852>.
- [40] E. Ising, Beitrag zur Theorie des Ferromagnetismus, *Z. Für Phys.* 31 (1) (1925) 253–258, <https://doi.org/10.1007/BF02980577>.
- [41] G.S. Joyce, Classical Heisenberg Model, *Phys. Rev.* 155 (2) (1967) 478–491, <https://doi.org/10.1103/PhysRev.155.478>.
- [42] S. Chib, E. Greenberg, Understanding the metropolis-Hastings algorithm, *Am. Stat.* 49 (1995) 327–335, <https://doi.org/10.2307/2684568>.
- [43] D.P. Landau, K. Binder, *A Guide to Monte Carlo Simulations in Statistical Physics*, Cambridge University Press, Cambridge, 2014.
- [44] D. Pletinckx, The use of quaternions for animation, modelling and rendering, in: *New Trends Comput. Graph.*, Springer, 1988, pp. 44–53.
- [45] D. Pletinckx, Quaternion calculus as a basic tool in computer graphics, *Vis. Comput.* 5 (1–2) (1989) 2–13, <https://doi.org/10.1007/BF01901476>.
- [46] S.K. Singhal, D.R. Cheriton, Exploiting position history for efficient remote rendering in networked virtual reality, *Presence Teleoperators Virtual Environ.* 4 (2) (1995) 169–193, <https://doi.org/10.1162/pres.1995.4.2.169>.
- [47] J. Diebel, Representing attitude: Euler angles, unit quaternions, and rotation vectors, *Matrix.* 58 (2006) 1–35.
- [48] W.R. Hamilton, LXXVIII. On quaternions; or on a new system of imaginaries in Algebra: to the editors of the Philosophical Magazine and Journal, Lond. Edinb. Dublin Philos. Mag. J. Sci. 25 (1844) 489–495, <https://doi.org/10.1080/1478644408645047>.
- [49] W.R. Hamilton, On a new species of imaginary quantities connected with a theory of quaternions, *Proc. R. Ir. Acad.* (1844) 4.1.
- [50] Z. Nehme, Y. Labaye, R. Sayed Hassan, N. Yaacoub, J.M. Grenache, Modeling of hysteresis loops by Monte Carlo simulation, *AIP Adv.* 5 (12) (2015) 127124, <https://doi.org/10.1063/1.4938549>.
- [51] A. Lüscher, A.M. Läuchli, Exact diagonalization study of the antiferromagnetic spin-1/2 Heisenberg model on the square lattice in a magnetic field, *Phys. Rev. B* 79 (2009), 195102, <https://doi.org/10.1103/PhysRevB.79.195102>.
- [52] J.M. Cook, Rational formulae for the production of a spherically symmetric probability distribution, *Math. Comput.* 11 (1957), 81–81. <https://doi.org/10.1090/S0025-5718-1957-0690630-7>.
- [53] G. Marsaglia, Choosing a Point from the Surface of a Sphere, *Ann. Math. Stat.* 43 (2) (1972) 645–646, <https://doi.org/10.1214/aoms/1177692644>.
- [54] Mervin E. Muller, A note on a method for generating points uniformly on n-dimensional spheres, *Commun. ACM.* 2 (4) (1959) 19–20, <https://doi.org/10.1145/377939.377946>.
- [55] E.W. Weisstein, Sphere point picking, *mathworld.wolfram.com*, 2002. [mathworld.wolfram.com](http://mathworld.wolfram.com).
- [56] H. Goldstein, The euler angles and Euler angles in alternate conventions, in: *Class. Mech.*, Addison-Wesley Reading, MA, 1980: pp. 143–148.
- [57] G.G. Slabaugh, Computing Euler angles from a rotation matrix, *City University London*, 1999.
- [58] E.W. Weisstein, Euler angles, *mathworld.wolfram.com*, 2009.
- [59] J.B. Kuipers, *Quaternions and Rotation Sequences*, Princeton University Press Princeton, 1999.
- [60] K. Shoemake, Animating Rotation with Quaternion Curves, in: *Proceedings of the 12th Annual Conference on Computer Graphics and Interactive Techniques*, ACM, New York, NY, USA, 1985: pp. 245–254. <http://doi.acm.org/10.1145/325334.325242> (accessed September 1, 2019).
- [61] Lars Onsager, A two-dimensional model with an order-disorder transition, *Phys. Rev.* 65 (3–4) (1944) 117–149, <https://doi.org/10.1103/PhysRev.65.117>.
- [62] George A. Baker, H.E. Gilbert, J. Eve, G.S. Rushbrooke, High-Temperature Expansions for the Spin-½ Heisenberg Model, *Phys. Rev.* 164 (2) (1967) 800–817, <https://doi.org/10.1103/PhysRev.164.800>.
- [63] R.Y. Diaz, Modeling of macroscopic anisotropies due to surface effects in magnetic thin films and nanoparticles, *Universidad Autónoma de Madrid* (2011).

- [64] Chengxi Huang, Junsheng Feng, Fang Wu, Dildar Ahmed, Bing Huang, Hongjun Xiang, Kaiming Deng, Erjun Kan, Toward intrinsic room-temperature ferromagnetism in two-dimensional semiconductors, *J. Am. Chem. Soc.* 140 (36) (2018) 11519–11525, <https://doi.org/10.1021/jacs.8b07879>.
- [65] Naihua Miao, Bin Xu, Linggang Zhu, Jian Zhou, Zhimei Sun, 2D intrinsic ferromagnets from van der Waals Antiferromagnets, *J. Am. Chem. Soc.* 140 (7) (2018) 2417–2420, <https://doi.org/10.1021/jacs.7b12976>.
- [66] Yinghe Zhao, Lingfang Lin, Qionghua Zhou, Yunhai Li, Shijun Yuan, Qian Chen, Shuai Dong, Jinlan Wang, Surface Vacancy-induced switchable electric polarization and enhanced ferromagnetism in monolayer metal trihalides, *Nano Lett.* 18 (5) (2018) 2943–2949, <https://doi.org/10.1021/acs.nanolett.8b00314>.